

Three-dimensional transitions in a swirling jet impinging against a solid wall at moderate Reynolds numbers

J. Ortega-Casanova and R. Fernandez-Feria

E. T. S. Ingenieros Industriales, Universidad de Málaga, Pza. El Ejido s/n, 29013 Málaga, Spain

(Received 19 December 2008; accepted 2 March 2009; published online 27 March 2009)

We consider the three-dimensional structure of a q -vortex interacting with a solid surface perpendicular to its axis. We use a direct numerical simulation based on a potential vector formulation with a Fourier decomposition in azimuthal modes for a Reynolds number equal to 100. This method is specially suited for the study of the nonlinear stability of axially symmetric flows because one may follow the raising of the different nonaxisymmetric modes from numerical noise, their nonlinear development, and their nonlinear interactions. For the given Reynolds number we find that there exists several transitions as the swirl number is increased, including the development of nonaxisymmetric instabilities for different azimuthal modes, and the formation of a vortex breakdown bubble that turns the flow axisymmetric again. We analyze these transitions and characterize them as a function of the swirl number for different distances of the incoming vortex to the wall. © 2009 American Institute of Physics. [DOI: 10.1063/1.3103364]

I. INTRODUCTION

A detailed knowledge of the different structures appearing in a swirling jet or wake as the governing parameters are varied, due to linear and nonlinear instabilities, and to other phenomena such as vortex breakdown, is crucial for several technical and industrial applications of this type of flows.¹ For instance, it is important in combustion systems to enhance mixing, reduce pollution, and for flame stabilization by taking advantage of the vortex breakdown phenomenon.^{2,3} It is also relevant in trailing vortices behind aircrafts to increase the possible take-off frequency at airports,^{4,5} or in vortices above a delta wing to prevent an abrupt deterioration of the lift and drag characteristics, and a poor controllability, of the aircraft.⁶

Impinging swirling jets are of interest in areas such as paper and fabric drying, local cooling of turbine blades and high-power electronics, material coating, metal solidification, and many others.⁷ The study in the present work has been motivated by yet another technical application of swirling jets such as seabed excavation. In this case one is interested in generating a flow recirculation zone attached to the seabed, together with an increase in the shear stress at the bed, to enhance the extraction of sediments from it. Vortex breakdown phenomenon is important to reach these objectives,⁸ but this phenomenon is strongly affected by non-axisymmetric, or three-dimensional (3D), instabilities of the swirling jet. This constitutes the main objective of the present work, namely, to characterize the appearance of 3D instabilities, and their nonlinear evolution as traveling waves, in a swirling jet impinging normally against a solid wall as the swirl parameter is increased for a given, moderately large Reynolds number of the jet. In this sense, the present work may be considered as a 3D extension of the axisymmetric flow considered in Ref. 8 for a similar swirling jet configuration. As we shall see, there exists a strong interaction between the recirculation region produced by the vortex break-

down phenomenon and the nonlinear waves generated by the 3D instabilities in the incoming swirling jet.

Of course, since the concentration of particles raised from the bed by the flow is usually very high, the interaction between the sediment particles and the swirling flow is essential in the characterization of the real process. However, to gain a first insight on the physics of the problem we consider here only the incompressible flow, without particles, and perform a series of 3D numerical simulations for the interaction of a quite general swirling jet, such as the q -vortex, with a solid surface normally to its axis of symmetry. In addition, owing to the high computer capacity required by 3D flow simulations, especially when 3D traveling waves have to be captured, we shall only consider a single Reynolds number of the jet (equal to 100). However for this Reynolds number we analyze the different flow structures arising as the swirl number is increased from 0 to 2.5, for several distances of the incoming vortex to the solid wall. We characterize the different 3D transitions of the flow as the swirl number is increased, and study how they are affected by the distance to the wall. Thus, for instance, we show that nonaxisymmetric instabilities modify the original axisymmetric flow above a critical swirl when the distance to the plate is sufficiently large, as in the unconfined vortex case, but these instabilities are suppressed for short distances to the wall. Also, that the vortex breakdown phenomenon, appearing above another critical swirl which depends on the distance to the wall, tends to suppress nonaxisymmetric perturbations.

3D numerical simulations, and nonlinear stability analyses, of swirling jets have been recently performed by several authors in quite different configurations (Refs. 9–12, among others). Although somewhat similar trends to those reported in these works are observed in the present simulations, no quantitative comparisons are possible because the differences in the structure of the incoming swirling jet and, more im-

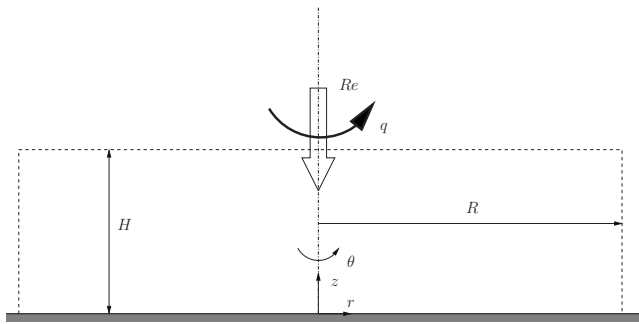


FIG. 1. Sketch of the nondimensional integration domain and coordinates.

portantly, in the global configuration of the flow due to the presence of the solid wall, which completely alters the swirling flow. We shall make use, however, of the abundant information about the linear stability of the q -vortex (also called Batchelor vortex; see, e.g., Ref. 13 for a general account, and Refs. 14–18 for more recent works), which constitutes the inlet velocity profile in the numerical simulations given here, to explain the appearance of the different instabilities. Our numerical method, based on a decomposition of the velocity field into symmetric and nonaxisymmetric parts, with a vector potential formulation for the nonaxisymmetric part,¹⁹ is able to capture these instabilities from just numerical noise, and to follow their development into nonlinear traveling waves, tracking their nonlinear interactions.

II. FORMULATION OF THE PROBLEM AND NUMERICAL METHOD

We consider in this work the interaction of a q -vortex with a solid surface perpendicular to its axis. In cylindrical polar coordinates (r, θ, z) , the velocity field (U, V, W) of this vortex is given by

$$U = 0, \quad V = \frac{q}{r}(1 - e^{-r^2}), \quad W = e^{-r^2}. \quad (1)$$

All the magnitudes are nondimensional: r is made dimensionless with a characteristic radius r_c (the dispersion radius of vorticity of the vortex), and the velocity field with a characteristic axial velocity W_c . The vortex is characterized by a swirl parameter,

$$q = \frac{V_c}{W_c}, \quad (2)$$

where V_c is a reference azimuthal velocity. This vortex with axial flow is a simplification of Batchelor's trailing-line vortex,²⁰ which is widely used in many vortex applications as a simple model because it is a good fit to the experimental velocity profiles for vane-guide-generated pipe vortices.^{21,22}

We solve the incompressible Navier–Stokes equations

$$\nabla \cdot \mathbf{v} = 0, \quad (3)$$

$$\frac{\partial \mathbf{v}}{\partial t} + \mathbf{v} \cdot \nabla \mathbf{v} = -\nabla p + \frac{1}{\text{Re}} \nabla^2 \mathbf{v}, \quad (4)$$

in the cylindrical domain depicted in Fig. 1, where

$$\text{Re} = \frac{r_c W_c}{\nu} \quad (5)$$

is the Reynolds number, with ν the kinematic viscosity of the fluid. Time t is made dimensionless with r_c/W_c , and the pressure p with ρW_c^2 , where ρ is the fluid density (however, the pressure will not enter explicitly in our formulation, see below).

The velocity field (1) is used as the inlet boundary condition on the plane $z=H$, but with a minus sign in the axial velocity W since the vortex propagates downward. We use $H=10$ for the detailed computations reported below, thus corresponding to a wall located ten vortex core radii downstream the inlet vortex; but we report all the relevant results for the wide range $2.5 \leq H \leq 15$. At the wall, $z=0$, the velocity \mathbf{v} vanishes, and at the cylindrical surface $r=R$ we use nonreflecting (radiation) boundary conditions (see below). R is chosen large enough for this last boundary condition not to affect the interaction of the vortex with the solid plane ($R=40$ in most of the computations reported in this work, but it has to be even larger for the highest swirl numbers considered). Note that owing to the radial decay of the q -vortex (1), the inlet surface $z=H$ behaves as a solid wall for large r .

To solve numerically the above problem, the velocity field is split into two parts, an axisymmetric base flow, $\mathbf{V}(r, z, t)$, plus a general perturbation field, $\mathbf{\Lambda}(r, \theta, z, t)$,

$$\mathbf{v}(r, \theta, z, t) = \mathbf{V}(r, z, t) + \mathbf{\Lambda}(r, \theta, z, t). \quad (6)$$

The axisymmetric flow is solved through the streamfunction-circulation-vorticity formulation (see, e.g., Ref. 23),

$$\begin{aligned} \mathbf{V} \equiv (U, V, W)^T &= \nabla \wedge (\psi \mathbf{e}_\theta) + \frac{1}{r} \Gamma \mathbf{e}_\theta \\ &= \left(-\frac{1}{r} \frac{\partial \psi}{\partial z}, \frac{1}{r} \Gamma, \frac{1}{r} \frac{\partial \psi}{\partial r} \right)^T, \end{aligned} \quad (7)$$

where ψ is the streamfunction, $\Gamma = rV$ the circulation, and the superscript T means transposed. The deviation velocity $\mathbf{\Lambda}$ is written in terms of the potential vector $\mathbf{\Psi}(r, \theta, z, t)$,

$$\mathbf{\Lambda} = \nabla \wedge \mathbf{\Psi}. \quad (8)$$

The fact that $\nabla \wedge \nabla \phi \equiv \mathbf{0}$ for any scalar function ϕ can be used to eliminate one of the components of $\mathbf{\Psi}$ (the θ -component, say) so that the potential vector can be written with just two components,²⁴

$$\mathbf{\Psi} = (\mathcal{G}, 0, \mathcal{F})^T. \quad (9)$$

Therefore, the complete velocity field can be written as

$$\mathbf{v} = \begin{pmatrix} -\frac{1}{r} \partial_z \psi \\ \frac{1}{r} \Gamma \\ \frac{1}{r} \partial_r \psi \end{pmatrix} + \begin{pmatrix} \frac{1}{r} \partial_\theta \mathcal{F} \\ \partial_z \mathcal{G} - \partial_r \mathcal{F} \\ -\frac{1}{r} \partial_\theta \mathcal{G} \end{pmatrix}, \quad (10)$$

where ∂_i means partial derivative with respect to the variable i . With this formulation, the continuity equation (3) is automatically satisfied.

To simplify the numerical solution of the equations and to eliminate the pressure from the formulation we use as intermediate variables the components of the vorticity field $\omega = \nabla \wedge \mathbf{v}$, which is also decomposed into axisymmetric and nonaxisymmetric parts in accordance with Eq. (10). The equations to be solved are then the θ -component of the momentum equation (4) for Γ , and the three components of the vorticity equations, together with the definitions of the vorticity components in terms of ψ , Γ , \mathcal{F} , and \mathcal{G} . More details of the numerical method, together with a test of its accuracy, are given in Ref. 19. Here we only give the specific information relevant for the present problem.

One of the main advantage of this numerical method is that one can easily follow the nonlinear evolution of the different nonaxisymmetric modes once the axisymmetric base flow is previously obtained. To that end, the variables describing the nonaxisymmetric part of the flow are discretized in the azimuthal direction θ by means of a complex Fourier decomposition, truncated at some finite azimuthal wavenumber N_θ . Thus, for instance, the two components of the vector potential are written as

$$\begin{aligned} \mathcal{F}(r, z, \theta, t) &= \sum_{n=-N_\theta, n \neq 0}^{n=N_\theta} \varphi_n(r, z, t) e^{in\theta}, \\ \mathcal{G}(r, z, \theta, t) &= \sum_{n=-N_\theta, n \neq 0}^{n=N_\theta} \chi_n(r, z, t) e^{in\theta}, \end{aligned} \quad (11)$$

where the axisymmetric mode $n=0$ is not included because it is transferred into the axisymmetric variables. Therefore, for each one of the nonaxisymmetric variables there are $2N_\theta$ unknown functions of (r, z, t) . However, taking into account that the velocity and vorticity fields are obviously real fields, it follows that $f_{-n} = \hat{f}_n$, $1 \leq n \leq N_\theta$, where f is any of the non-axisymmetric scalar variables and the hat denotes complex conjugate. This halves the number of unknown functions and equations associated to each nonaxisymmetric variable. The total number of dependent variables and equations is thus $5N_\theta + 3$; i.e., the three axisymmetric variables (stream function ψ , circulation Γ , and axisymmetric part of the azimuthal vorticity component $\eta \equiv \partial_z U - \partial_r W$),²³ and the N_θ modes of the two components of the vector potential plus the three components of the nonaxisymmetric part of the vorticity. These equations, together with the boundary conditions, are discretized in $N_r + 1$ nodes in the radial direction and $N_z + 1$ nodes in the axial direction. In particular, in the radial direction a Chebyshev pseudospectral collocation method²⁵ is used, while in the axial direction we use a second order finite-difference scheme on a nonuniform grid,²⁶ concentrating the nodes in the regions where the radial and axial gradients of the variables are the greatest. In the computations reported here we use N_θ between 3 and 12, N_r between 100 and 200, and N_z between 50 and 120, depending on H and R .

These values are adjusted in such a way that the accuracy of the results does not change practically when increasing them.

As indicated above, the boundary conditions are given by the axisymmetric velocity field (1) at $z=H$, with all the nonaxisymmetric variables set equal to zero, $\mathbf{v}=\mathbf{0}$ at the solid wall $z=0$, and regularity conditions at the axis $r=0$. At the outflow boundary $r=R$ we use the usual quasicylindrical flow conditions for the axisymmetric ($n=0$) variables, i.e., second order radial derivatives equal to zero (see, e.g., Refs. 27 and 28), and a nonreflecting (radiation) boundary condition for the nonaxisymmetric variables.^{29,30} We have set $R=40$ initially, which is large enough for the computed axisymmetric flow to be independent of the boundary conditions, but it has to be increased for high swirl numbers due to the increasing size of the vortex breakdown bubble. Nonreflecting boundary conditions allow for the free exit of the nonaxisymmetric perturbations that may appear inside the flow through the outlet section, avoiding numerical instabilities or spurious wave reflections at $r=R$.³⁰

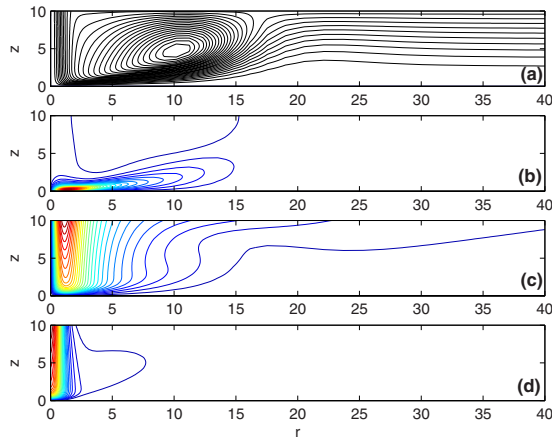
As for the numerical scheme for solving the temporal evolution of the flow variables, we first obtain the axisymmetric flow by solving the equations governing the axisymmetric variables, setting all the nonaxisymmetric variables equal to zero. The numerical procedure is very similar to that described in Ref. 23: Given the solution at a given instant $t = \tau \Delta t$, where Δt is the time step, the temporal derivatives in the equations are approximated with a semi-implicit, two step predictor-corrector scheme with second order error in time. Viscous terms in these equations are discretized implicitly, while the convective terms explicitly. The numerical procedure is started at $t=0$ from the flow at rest until an axisymmetric steady state is reached. Once this axisymmetric steady state is obtained, we solve the whole set of 3D equations with initial conditions given by the steady axisymmetric flow for the axisymmetric variables ψ , Γ , and η , and random noise with a given intensity level $\varepsilon \ll 1$ for all the nonaxisymmetric variables (we use $\varepsilon = 10^{-5}$ in most of the reported computations given below). The temporal derivatives in the parabolic evolution equations are approximated in the same way as describe above for the axisymmetric variables, and the Poisson-like equations are solved by means of an iterative successive over-relaxation scheme, for which the optimum value of the under-relaxation factor is obtained with some preliminary tests. The time step in the computations reported below is 0.01.

III. RESULTS AND DISCUSSION

A. Results for $H=10$

We report here with some detail the results for $\text{Re}=100$, $H=10$, and for increasing values of the swirl parameter q . The results for different values of H are summarized in Sec. III B.

We present first the results for the steady axisymmetric flow (for ψ , U , V , and W), which is used as the initial condition for the 3D numerical simulation, and then for the temporal evolution of the 3D flow. To this end we shall plot contour lines in different planes of the three components of the perturbation velocity $\mathbf{\Lambda}$, given by



$$\Lambda_r = \frac{1}{r} \partial_\theta \mathcal{F} \approx \frac{1}{r} \Re \left[\sum_{n=-N_\theta, n \neq 0}^{N_\theta} n \varphi_n e^{in\theta} \right], \quad (12)$$

$$\Lambda_\theta = \partial_z \mathcal{G} - \partial_r \mathcal{F} \approx \Re \left[\sum_{n=-N_\theta, n \neq 0}^{N_\theta} (\partial_z \chi_n - \partial_r \varphi_n) e^{in\theta} \right], \quad (13)$$

$$\Lambda_z = -\frac{1}{r} \partial_\theta \mathcal{G} \approx -\frac{1}{r} \Re \left[\sum_{n=-N_\theta, n \neq 0}^{N_\theta} n \chi_n e^{in\theta} \right], \quad (14)$$

at some instants of time, in addition to the temporal evolution of some significant nonaxisymmetric variables. In particular, the nonlinear evolution of the different azimuthal modes will be characterized by the maximum in the whole flow domain of the modulus of the n th mode of the azimuthal perturbation velocity component,

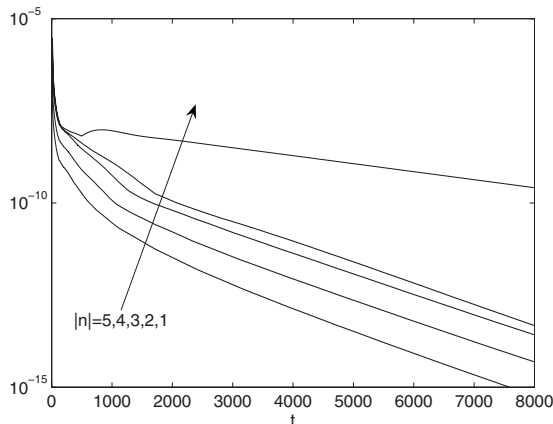


FIG. 3. Temporal evolution of $\max|\Lambda_{\theta,n}|$ in the whole flow domain, with $|n|=1, \dots, 5$, as indicated, for $Re=100$, $H=10$, and $q=0.1$.

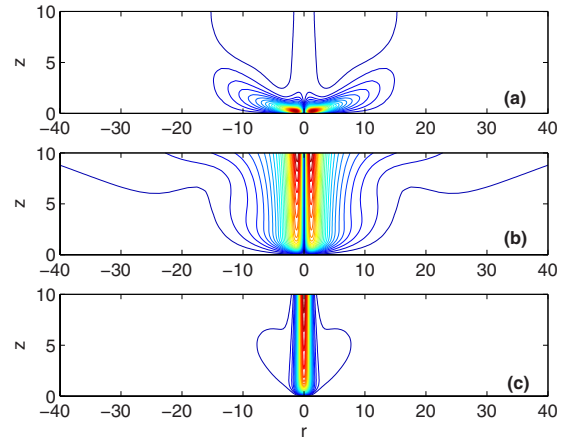


FIG. 4. (Color online) Contour lines of the radial velocity u (a), the azimuthal velocity v (b), and the axial velocity w (c) in the axial planes $\theta=0(r>0)$ and $\theta=\pi(r<0)$ for $Re=100$, $H=10$, $q=0.1$, and $t=8221$. 30 equidistant contours are plotted between -0.021 27 and 0.016 74 in (a), 0 and 0.0022 in (b), and -0.019 63 and 0.035 16 in (c).

$$\max|\Lambda_{\theta,n}(t)| \equiv \max_{r,z} |\partial_z \chi_n(r, z, t) - \partial_r \varphi_n(r, z, t)|. \quad (15)$$

The temporal behavior of the radial and axial components, $\max|\Lambda_{r,n}(t)|$ and $\max|\Lambda_{z,n}(t)|$, are quite similar to $\max|\Lambda_{\theta,n}(t)|$ and will not be shown.

For $Re=100$, the inlet q -vortex is convectively unstable to helical perturbations with azimuthal wavenumber $n=-1$ for all values of the swirl parameter in the range $0 < q < 1.08$.¹³ Obviously, the parallel-flow assumption used in the stability analysis of Ref. 13 is not valid in the present jet flow impinging against a solid wall, but, since the plate is relatively far from the flow inlet in terms of the vortex core size, similar convective instabilities with $n=-1$ are observed in our numerical simulations for $q \lesssim 0.4$. However, the amplitude of the resulting traveling waves do not grow enough before reaching the vicinity of the wall, and their amplitudes remain so small that the computed flow is practically axisymmetric.

This behavior can be observed in Figs. 2–6 for $q=0.1$.

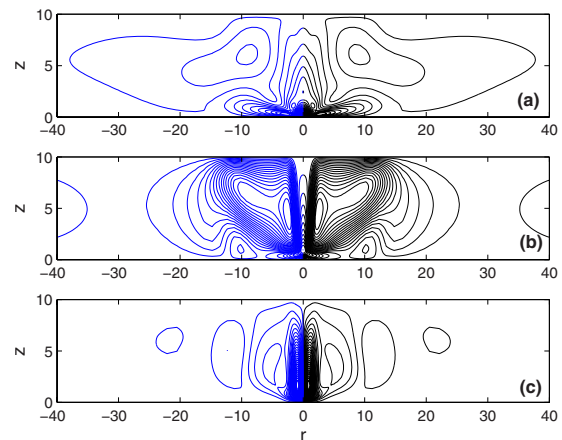


FIG. 5. (Color online) Contour lines of Λ_r (a), Λ_θ (b), and Λ_z (c) in the axial planes $\theta=0(r>0)$ and $\theta=\pi(r<0)$ for $Re=100$, $H=10$, $q=0.1$, and $t=8221$. 60 equidistant contours are plotted between $\pm 4.652 \times 10^{-10}$ in (a), $\pm 1.136 \times 10^{-11}$ in (b), and $\pm 3.15 \times 10^{-11}$ in (c).

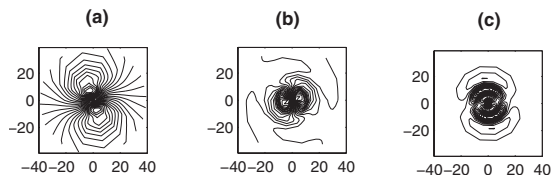


FIG. 6. Contour lines of Λ_r (a), Λ_θ (b), and Λ_z (c) in the (r, θ) -plane $z=4.8$ for $Re=100$, $H=10$, $q=0.1$, and $t=8221$. Spacing between contours is 1.6×10^{-11} , starting from -2.326×10^{-11} , in (a), 1.575×10^{-11} , starting from -2.283×10^{-10} , in (b), and 1.613×10^{-11} , starting from -2.34×10^{-10} , in (c).

The initial flow is the axisymmetric flow, depicted in Fig. 2, plus a perturbation of constant value $\varepsilon=10^{-5}$ for all the non-axisymmetric variables. As it is observed in Fig. 3, all these perturbations decay first very fast, and then more gradually. $|n|=1$ is the less stable mode, as predicted by the stability analysis (but now the numerically simulated flow is stable), with the amplitude of modes $|n|=2, 3, 4, 5$ remaining five or more orders of magnitude smaller than that of the mode $|n|=1$ as the flow evolves in time. Note also that $N_\theta=5$ azimuthal modes are more than enough to describe the flow in this case, because all the azimuthal modes decay very fast. Actually, $N_\theta=1$ would have been enough in this case. Thus, the flow remains practically axisymmetric (compare the flow at $t=8221$ in Fig. 4 with the axisymmetric initial flow in Fig. 2). Nonetheless, perturbations with $|n|=1$ are present in the flow, as observed in Figs. 5 and 6, but with very small amplitudes, of the order of 10^{-10} at that instant of time. These figures also show that the numerical method is able to capture organized flow structures with very small amplitudes. Remember that the initial noise to start the nonaxisymmetric variables is of the order of 10^{-5} , and that the 3D flow evolves to an organized structure, with $|n|=1$ as the dominant mode (clearly observed in Fig. 6), of much smaller amplitude.

The situation is quite similar for $q=0.4$ (see Figs. 7–10), but in this case the amplitude of the mode $|n|=1$ remains constant after the initial decay from the starting noise (see Fig. 8; note that we now use $N_\theta=8$ azimuthal nodes, as in most of the computations reported below). The perturbations

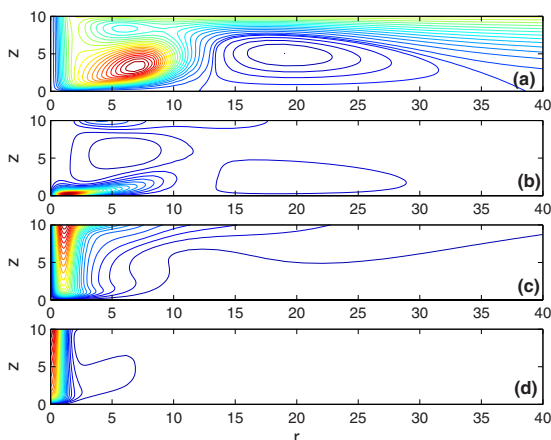


FIG. 7. (Color online) As in Fig. 2 but for $q=0.4$. The spacing between contours is 0.0388, starting from -0.171 , in (a), 0.014 78, starting from -0.0301 , in (b), 0.0088, starting from 0 at the axis, in (c), and 0.035 52, starting from -0.03 , in (d).

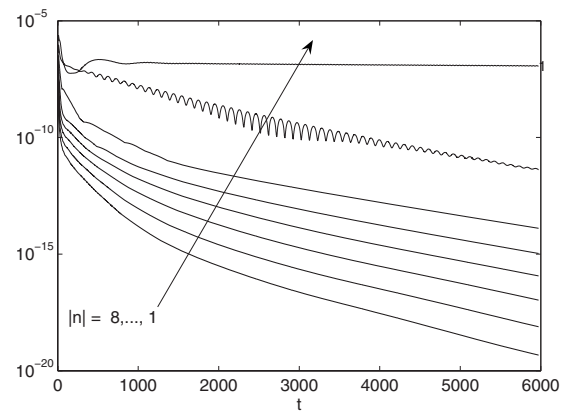


FIG. 8. As in Fig. 3, but for $q=0.4$ and $|n|=1, \dots, 8$.

have a clear helical structure with $|n|=1$ (Figs. 9 and 10). However the amplitude is still too small (of the order of 10^{-7} now) to modify the axisymmetric flow in a perceptible way.

The simulated flow change substantially for q slightly larger than 0.4. In particular, for $q \approx 0.43$, the flow becomes unstable for the azimuthal mode $|n|=2$, and the final state is clearly nonaxisymmetric. This behavior remains qualitatively the same in the wide range of swirl numbers $0.43 \lesssim q \lesssim 0.96$, and we find that it is associated to an *absolute* instability of the axisymmetric flow. This is based on the fact that the parallel q -vortex with $Re=100$ is absolutely unstable for perturbations with $|n|=2$ in the interval $0.4 \lesssim q \lesssim 0.5$.³¹

For instance, Fig. 11 shows the spatial stability properties of the parallel q -vortex for $Re=100$ and $q=0.45$. In particular, it is shown the dispersion relation in terms of the spatial growth rate as a function of the frequency, $\gamma(\omega)$, and the axial wavenumber as a function of the frequency, $\alpha(\omega)$, for different azimuthal wavenumbers n [see Ref. 17 for the exact definitions of $\gamma(\omega)$ and $\alpha(\omega)$, and for the details of the stability analysis]. It is observed that the mode $|n|=2$ has reached the onset of absolute instability from a spatial stability point of view, with a cusp point in γ for $|\omega| \approx 0.13$, and vanishing group velocity $\partial\omega/\partial\alpha$ at that frequency.³² Al-

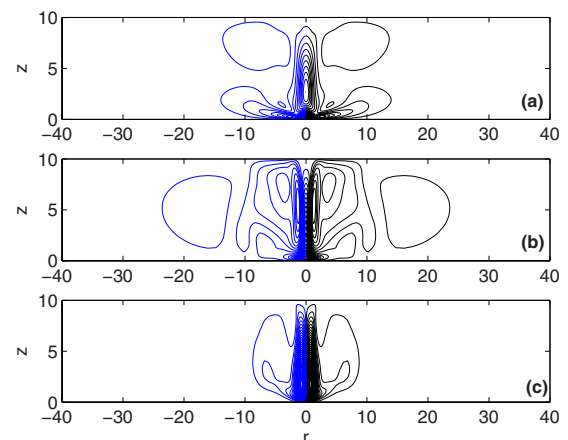


FIG. 9. (Color online) As in Fig. 5, but for $q=0.4$ at $t=5973$. 60 equidistant contours are plotted between $\pm 2.02 \times 10^{-7}$ in (a), $\pm 1.1 \times 10^{-7}$ in (b), and $\pm 2.09 \times 10^{-7}$ in (c).

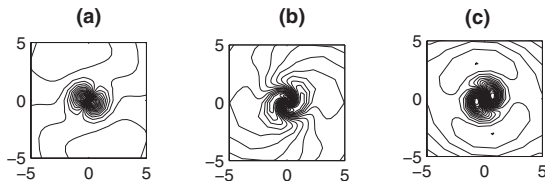


FIG. 10. As in Fig. 6, but for $q=0.4$ at $t=5973$. Spacing between contours is 7.90×10^{-9} , starting from -1.14×10^{-7} , in (a), 7.775×10^{-9} , starting from -1.13×10^{-7} , in (b), and 7.922×10^{-9} , starting from -1.15×10^{-7} , in (c).

though the present inlet q -vortex becomes almost immediately distorted downstream of the flow inlet due to the presence of the wall, and nonparallel effects become important on any stability analysis of the flow, the properties of the numerically simulated flow for $q=0.45$ (Figs. 12–16) agree very well with this absolute instability. The initial axisymmetric flow (Fig. 12) becomes clearly nonaxisymmetric for $t \geq 2000$ (see Fig. 13), the amplitude of the final 3D perturbations being now of the order of 10^{-1} (Figs. 13–16). The dominant mode is clearly $|n|=2$, as observed in Figs. 14 and 16, and the frequency of the oscillations is about 0.08 (Fig. 13), close to the value obtained from the *parallel* flow stability analysis.

What is more relevant for the present nonlinear stability analysis is the way in which this 3D flow evolves in time (see Fig. 14). As in the previous cases, the amplitude of the initial noise, of the order of 10^{-5} , first decay in time. Now, just after this short transient interval, the amplitude of the mode $|n|=2$ starts increasing in an exponentially way (linearly in the logarithmic plot of Fig. 14), therefore as a consequence of a linear instability. This (absolute) instability is originated near the axis, inside the core of the jet, approximately at the middle plane between the inlet q -vortex and the wall. Much before this instability saturates, nonlinear interactions take place among the different azimuthal modes with even values of n , that also become unstable. This is because the wavenumber 2 solution has energy in its harmonics, i.e., in all even Fourier modes. However, just after these even

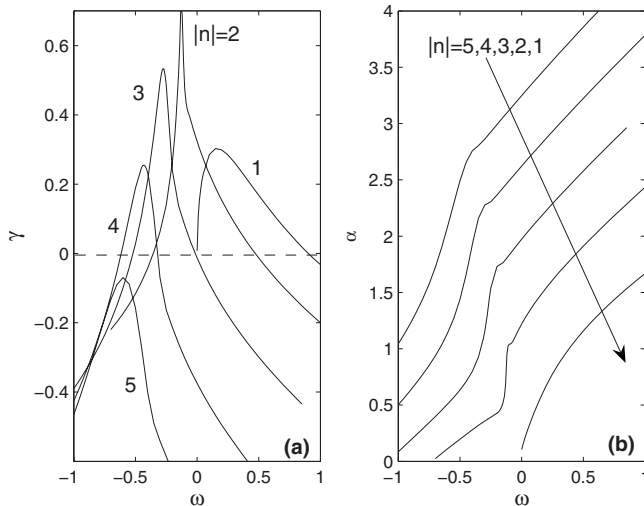


FIG. 11. Spatial growth rate γ (a), and axial wavenumber α (b) as functions of the frequency ω for a q -vortex with $Re=100$ and $q=0.45$.

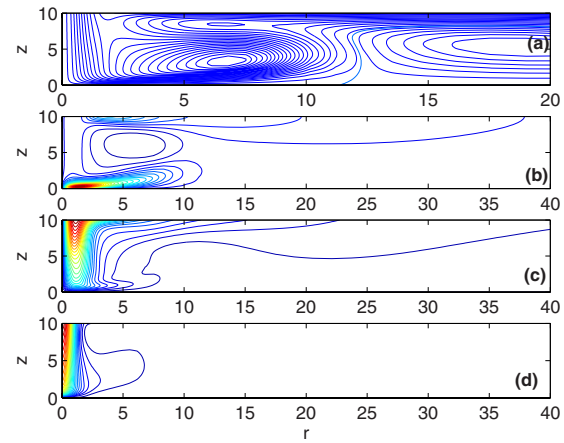


FIG. 12. (Color online) As in Fig. 2 but for $q=0.45$. Note that only $0 \leq r \leq 20$ is plotted. 30 equidistant contours between -0.28 and 0.971 in (a), -0.033 and 0.3183×10^{-2} in (b), 0 and 0.2872 in (c), and -0.0324 and 1 in (d).

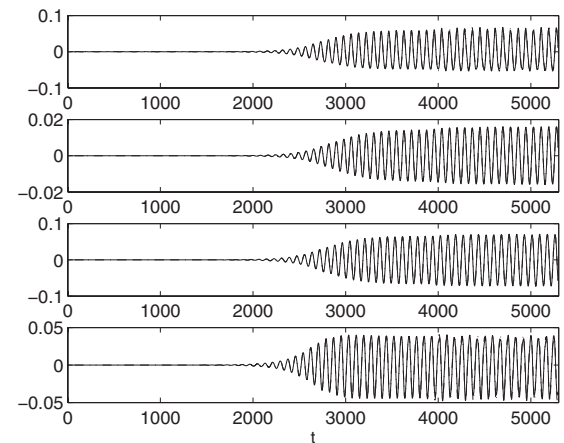


FIG. 13. Temporal evolution of the radial velocity perturbation Λ_r at $\theta=0$ (continuous lines) and $\theta=\pi$ (dashed lines), $r=1$, and the axial locations (from top to bottom) $z=1.38, 5, 3.5,$ and 9.46 , for $Re=100, q=0.45$. Since the dominant azimuthal mode is even, the lines at $\theta=0$ and $\theta=\pi$ practically coincide.

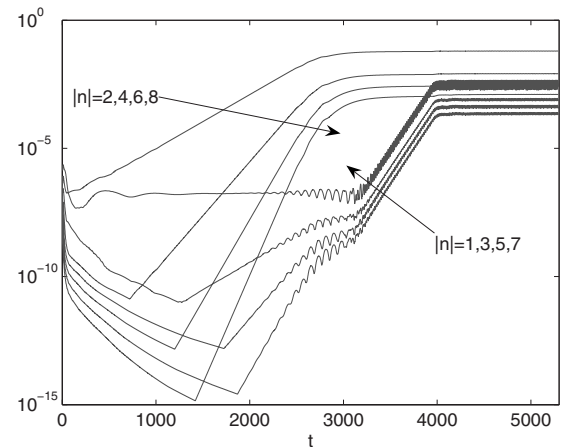


FIG. 14. As in Fig. 3, but for $q=0.45$.

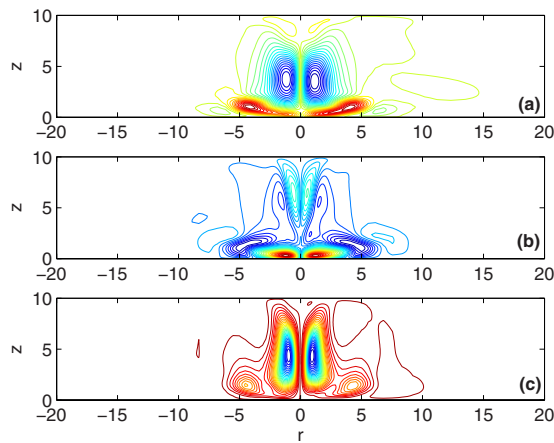


FIG. 15. (Color online) As in Fig. 5, but for $q=0.45$ at $t=5293$. 60 equidistant contours are plotted between -7.09×10^{-2} and 5.22×10^{-2} in (a), -3.97×10^{-2} and 1.18×10^{-1} in (b), and -1.44×10^{-1} and -1.49×10^{-1} in (c).

modes saturate, a new bifurcation occurs in which the mode $|n|=1$ becomes unstable and, consequently, all the Fourier modes. At the end, all the modes become saturated, reaching the flow an oscillatory (traveling waves) state, with a velocity perturbation structure dominated by the azimuthal mode $|n|=2$ (see Figs. 14–16), whose amplitude is almost one order of magnitude larger than the next (nonlinearly) unstable mode with $|n|=4$.

This scenario is a typical consequence of a double Hopf bifurcation of the original axisymmetric flow, where two distinct Hopf bifurcations occur, the first one for mode $|n|=2$ and its harmonics, and then for $|n|=1$ and all the Fourier modes (see Refs. 33–37 for some related examples in an enclosed swirling flow in which a detailed analysis of these Hopf bifurcations are presented).

A qualitatively similar behavior of the flow is found numerically for increasing values of q , until it becomes close to unity (more precisely, until $q \approx 0.96$). As shown in Fig. 17 for $q=1$, vortex breakdown takes place at the axis, with a stagnation point (zero axial velocity) at $z=8$. As a consequence, the 3D instabilities observed for smaller values of q disappear (Fig. 18). Thus, the formation of a breakdown region with flow recirculation, which is quite large in the present case (see Fig. 17), suppress nonaxisymmetric instabilities, and all the eight azimuthal modes considered in the present numerical simulation for $q=1$ decay in time from their initial small values (Fig. 18).

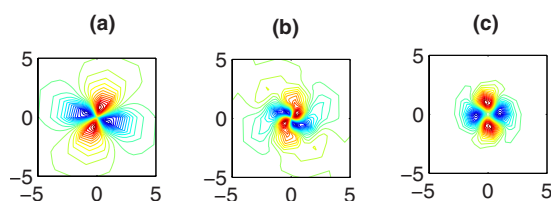


FIG. 16. (Color online) As in Fig. 6, but for $q=0.45$ at $t=5293$. 30 equidistant contours between -8.89×10^{-2} and 8.41×10^{-2} in (a), -1.28×10^{-1} and 1.216×10^{-2} in (b), and -1.795×10^{-1} and 1.91×10^{-1} in (c).

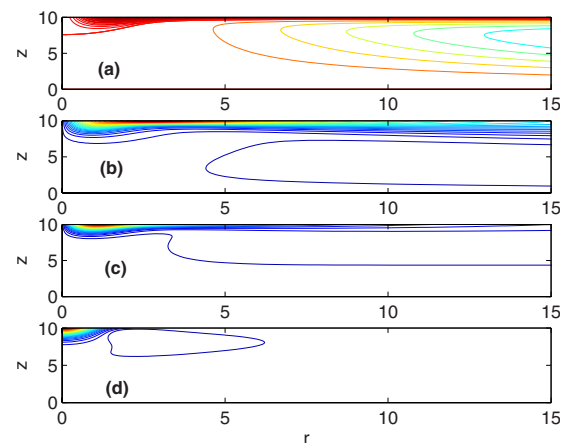


FIG. 17. (Color online) As in Fig. 2 but for $q=1.0$. Note that only $0 \leq r \leq 15$ is plotted. 20 equidistant contours are plotted in (a) between 0 and 0.5, and 10 between -2.87 and 0, 30 contours are plotted between -0.026 and 0.40 in (b), between 0 and 0.6382 in (c), and between -0.062 and 1 in (d).

As q increases further, the only significant difference is that the breakdown region with flow recirculation increases in size, with the stagnation point moving toward the flow inlet. However the flow remains stable to nonaxisymmetric perturbation, at least until the quite large swirl number $q=2.5$, which is the maximum value for which we have made numerical simulations. For these large values of q we have to increase the radial size R in the computations. We find that all the 3D perturbations are suppressed by the recirculating breakdown bubble, as in the case with $q=1$ reported above, and the flow remains axisymmetric.

B. Summary of results for different values of H

The computations have been repeated for different distances H to the wall in the range $2.5 \leq H \leq 15$. For $5.5 \leq H \leq 15$ the results are qualitatively similar to those reported above for $H=10$. There exists a first critical swirl $q_1(H)$ such that for $q < q_1(H)$ the flow remains practically axisymmetric. For $q_1(H) \leq q < q_2(H)$ the flow becomes absolutely unstable, first for perturbations with $|n|=2$, and then for rest of the azimuthal modes, with traveling waves propa-

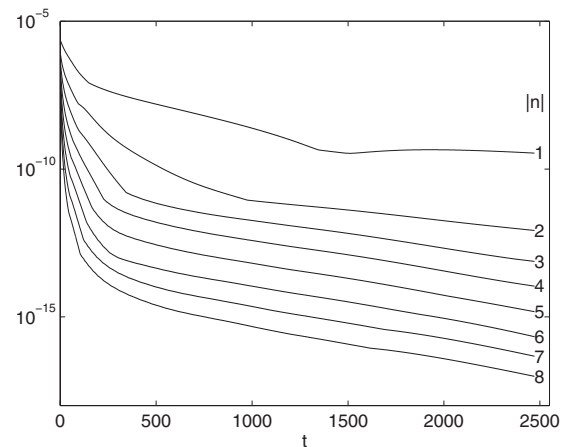
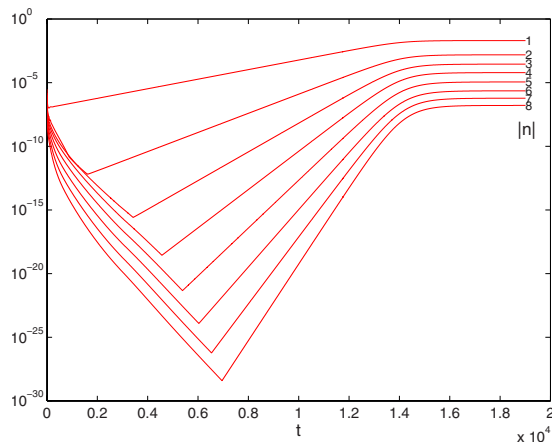


FIG. 18. As in Fig. 3, but for $q=1.0$.

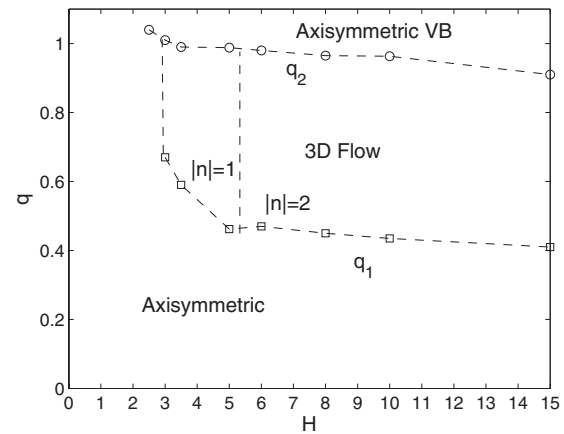
FIG. 19. (Color online) As in Fig. 3, but for $H=5$ and $q=0.5$.

gating downstream and transforming the original axisymmetric flow into a strongly nonaxisymmetric one. In these 3D flows the mode $|n|=2$ is always the dominant one. For $q \geq q_2(H)$, these 3D nonlinear perturbations become suppressed due to the formation of a vortex breakdown bubble above the critical value $q_2(H)$, in such a way that the flow becomes axisymmetric again, and remains so for all the swirl numbers larger than q_2 considered (up to $q=2.5$). The only differences with the case $H=10$ analyzed above reside in the quantitative values of critical swirl numbers q_1 and q_2 for the transitions, which are plotted in Fig. 20 for several values of H .

When $3 \leq H \leq 5.5$, we find that the dominant absolute instability arising for $q \geq q_1(H)$ does not correspond to perturbations with $|n|=2$, as in the previous cases, but with $|n|=1$. This behavior can be seen in Fig. 19 for $H=5$ and $q=0.5$, which is slightly larger than $q_1(H=5) \approx 0.46$, where it is observed that the mode $|n|=1$ starts growing exponentially after a short initial decay from the original noise, increasing its amplitude more than four orders of magnitude, and then saturates. Before that saturation, all the remaining modes also grow exponentially by nonlinear interactions, and then saturate. The final state is dominated by the helical mode $|n|=1$, whose amplitude is approximately one order of magnitude larger than the mode $|n|=2$, and this is about one order of magnitude larger than $|n|=3$, and so on. This is a consequence of the fact that now the Hopf bifurcation breaking the axial symmetry of the flow is for the $|n|=1$ mode, which has energy in all Fourier modes.

This behavior indicates that the stability properties of the incoming q -vortex are now strongly affected by the close presence of the flat plate, differing qualitatively from the stability properties of the unconfined vortex case. In other words, for a distance to the plate larger than approximately 5.5 times the vortex core, the impinging jet behaves qualitatively as a free vortex from a stability point of view. On the other hand, the vortex breakdown transition arising when $q \geq q_2(H)$ is qualitatively similar to the previous cases, with the flow becoming axisymmetric again for these swirl numbers (see Fig. 20 for the critical swirl values).

Finally, for $H \leq 3$ the influence of the wall on the swirling jet is so strong that the flow never becomes (absolutely)

FIG. 20. Critical swirl numbers q_1 (squares) and q_2 (circles) for several values of H . We also indicate the dominant azimuthal mode arising at $q_1(H)$.

unstable to nonaxisymmetric perturbations, because $q_1(H)$ becomes larger than $q_2(H)$, and therefore remaining axisymmetric for all the values of q considered. The transition to vortex breakdown for $q \geq q_2(H)$ is always present, at least for the values of $H \geq 2.5$ considered here, with q_2 increasing slightly as H decreases.

These different regions in the plane (H, q) , with different flow properties, are marked in Fig. 20.

IV. CONCLUSIONS

We have considered in this paper the interaction of a q -vortex impinging against a solid wall perpendicular to its axis at different distances H from the vortex inlet, for a Reynolds number equal to one hundred, and for increasing values of the swirl number (from 0 to 2.5). H measures the distance to the plate in terms of the vortex core radius, and we have considered values in the interval $2.5 \leq H \leq 15$. The first main conclusion is that instabilities in the nonlinear regime are generated from absolute instabilities of the axisymmetric incoming vortex above a critical swirl number q_1 , which depends on H (and, of course, on Re). For the Reynolds number considered, and for sufficiently large values of H , this instability corresponds to the azimuthal mode $|n|=2$, in agreement with the absolute instability of the unconfined q -vortex. Nonlinear mode interactions take place for $q \geq q_1$, and all the azimuthal modes become unstable, but with $|n|=2$ remaining always the dominant azimuthal mode. This behavior is a consequence of a double Hopf bifurcation, similar to the ones described by Lopez and co-workers in an enclosed swirling flow.^{33–37} For $H \leq 5.5$, the qualitative instability properties of the flow change due to the close presence of the wall, and the dominant absolute instability arising for $q \geq q_1(H)$ corresponds to perturbations with $|n|=1$, which in the nonlinear regime has energy in all the azimuthal modes. For $H \leq 3$ this absolute instability (bifurcation) disappears altogether, and the flow remains axisymmetric for all the values of the swirl number at the present Re .

The second main conclusion of this work is that there exists another critical swirl number $q_2(H)$, larger than $q_1(H)$ when q_1 exists, above which a stagnation point is formed at some point in the axis with a wide region of flow recircula-

tion downstream. The most significant consequence of the formation of this vortex breakdown bubble is that nonaxisymmetric instabilities become suppressed so that the flow becomes axisymmetric again for $q \geq q_2$. This axisymmetric vortex breakdown flow has been obtained even for the highest swirl number considered, $q=2.5$, differing only in the size of the breakdown bubble, which increases with q . For $H \leq 3$ the flow remains always axisymmetric because $q_1(H)$ becomes larger than $q_2(H)$ so that the vortex breakdown transition appears before any absolute instability as q is increased, impeding the formation of 3D traveling waves. All the critical swirl numbers q_1 and q_2 are summarized in Fig. 20 as functions of H for $Re=100$. This figure also summarizes the main qualitative differences between an impinging swirling jet and a free one as the distance H between the injection section and the wall decreases for a given Reynolds number.

This overall behavior of the flow as the swirl number is increased has been corroborated for other Reynolds number of the order of one hundred (in particular, for $Re=75$ and 200), but not enough computations have been performed to characterize with sufficient precision the critical swirl numbers as functions of Re and H owing to the high numerical cost of the 3D simulations. We think that the relevant result here is the interplay between nonaxisymmetric, nonlinear instabilities with the vortex breakdown phenomenon in this flow for moderate Reynolds numbers, showing the existence of a window of swirl numbers between q_1 and q_2 , where the flow is nonaxisymmetric (3D), if H is not too small. For $q > q_2$ the flow is practically axisymmetric, with a large region of flow recirculation. These results may be of practical interest in studying seabed excavation processes.

ACKNOWLEDGMENTS

This research has been supported by the Ministerio de Educación y Ciencia of Spain (Grant No. FIS2007-60161) and by the European Commission (Grant No. COOP-CT-2005-017725). The numerical computations were performed in the computer facility "Taylor" at the ETSII of the University of Málaga.

¹M. Escudier, "Confined vortices in flow machinery," *Annu. Rev. Fluid Mech.* **19**, 27 (1987).

²A. H. Lefebvre, *Gas Turbine Combustion*, 2nd ed. (Taylor and Francis, New York, 1999).

³J. Ji and J. P. Gore, "Flow structure in lean premixed swirling combustion," *Proc. Combust. Inst.* **29**, 861 (2002).

⁴L. Jacquin, D. Fabre, P. Gefroy, and E. Coustols, "The properties of a transport aircraft wake in the extended nearfield: An experimental study," AIAA Paper No. 2001-1038, 39th Aerospace Sciences Meeting and Exhibit, Reno, NV, 8–11 January 2001.

⁵T. Gerz, F. Holzapfel, W. Bryant, F. Kopp, M. Frech, A. Tafferner, and G. Winckelmans, "Research towards a wake-vortex advisory system for optimal aircraft spacing," *C. R. Phys.* **6**, 501 (2005).

⁶A. Mitchell and J. Delery, "Research into vortex breakdown control," *Prog. Aerosp. Sci.* **37**, 385 (2001).

⁷S. V. Alekseenko, A. V. Bilsky, V. M. Dulin, and D. M. Markovich, "Experimental study of an impinging jet with different swirl rates," *Int. J. Heat Fluid Flow* **28**, 1340 (2007).

⁸M. A. Herrada, C. del Pino, and J. Ortega-Casanova, "Confined swirling jet impingement on a flat plate at moderate Reynolds numbers," *Phys. Fluids* **21**, 013601 (2009).

⁹M. R. Ruith, P. Chen, E. Meiburg, and T. Maxworthy, "Three-dimensional vortex breakdown in swirling jets and wakes: Direct numerical simulation," *J. Fluid Mech.* **486**, 331 (2003).

¹⁰I. Delbende and M. Rossi, "Nonlinear evolution of a swirling jet instability," *Phys. Fluids* **17**, 044103 (2005).

¹¹M. A. Herrada and R. Fernandez-Feria, "On the development of 3D vortex breakdown in cylindrical regions," *Phys. Fluids* **18**, 084105 (2006).

¹²E. Sanmiguel-Rojas, M. A. Burgos, C. del Pino, and R. Fernandez-Feria, "Three-dimensional structure of confined swirling jets at moderately large Reynolds numbers," *Phys. Fluids* **20**, 044104 (2008).

¹³E. W. Mayer and K. G. Powell, "Viscous and inviscid instabilities of a trailing vortex," *J. Fluid Mech.* **245**, 91 (1992).

¹⁴C. Olendraru, A. Sellier, M. Rossi, and P. Huerre, "Inviscid instability of the Batchelor vortex: Absolute-convective transition and spatial branches," *Phys. Fluids* **11**, 1805 (1999).

¹⁵D. Fabre and L. Jacquin, "Viscous instabilities in trailing vortices at large swirl numbers," *J. Fluid Mech.* **500**, 239 (2004).

¹⁶C. J. Heaton, "Centre modes in inviscid swirling flows and their application to the stability of the Batchelor vortex," *J. Fluid Mech.* **576**, 325 (2007).

¹⁷L. Parras and R. Fernandez-Feria, "Spatial stability and the onset of absolute instability of Batchelor vortex for high swirl numbers," *J. Fluid Mech.* **583**, 27 (2007).

¹⁸S. Le Dizès and D. Fabre, "Large-Reynolds-number asymptotic analysis of viscous centre modes in vortices," *J. Fluid Mech.* **585**, 153 (2007).

¹⁹J. Ortega-Casanova and R. Fernandez-Feria, "A numerical method for the study of nonlinear stability of axisymmetric flows based on the vector potential," *J. Comput. Phys.* **227**, 3307 (2008).

²⁰G. K. Batchelor, "Axial flow in trailing line vortices," *J. Fluid Mech.* **20**, 645 (1964).

²¹A. K. Garg and S. Leibovich, "Spectral characterization of vortex breakdown flowfields," *Phys. Fluids* **22**, 2053 (1979).

²²S. Leibovich, "Vortex stability and breakdown: Survey and extension," *AIAA J.* **22**, 1192 (1984).

²³J. M. Lopez and P. D. Weidman, "Stability of stationary endwall boundary layers during spin-down," *J. Fluid Mech.* **326**, 373 (1996).

²⁴H. F. Goldstein, E. Knobloch, I. Mercader, and M. Net, "Convection in a rotating cylinder. Part I: Linear theory for moderate Prandtl numbers," *J. Fluid Mech.* **248**, 583 (1993).

²⁵C. Canuto, M. Y. Hussaini, A. Quarteroni, and T. A. Zang, *Spectral Methods in Fluid Dynamics* (Springer-Verlag, New York, 1988).

²⁶E. Sanmiguel-Rojas, J. Ortega-Casanova, C. del Pino, and R. Fernandez-Feria, "A Cartesian grid finite-difference method for 2d incompressible viscous flows in irregular geometries," *J. Comput. Phys.* **204**, 302 (2005).

²⁷P. Beran and F. Culik, "The role of nonuniqueness in the development of vortex breakdown in tubes," *J. Fluid Mech.* **242**, 491 (1992).

²⁸J. M. Lopez, "On the bifurcation structure of axisymmetric vortex breakdown in a constricted pipe," *Phys. Fluids* **6**, 3683 (1994).

²⁹G. Jin and M. Braza, "A nonreflecting outlet boundary condition for incompressible unsteady Navier–Stokes calculations," *J. Comput. Phys.* **107**, 239 (1993).

³⁰M. R. Ruith, P. Chen, and E. Meiburg, "Development of boundary conditions for direct numerical simulations of three-dimensional vortex breakdown in semi-infinite domains," *Comput. Fluids* **33**, 1225 (2004).

³¹C. Olendraru and A. Sellier, "Viscous effects in the absolute-convective instability of the Batchelor vortex," *J. Fluid Mech.* **459**, 371 (2002).

³²R. Fernandez-Feria and C. del Pino, "The onset of absolute instability of rotating Hagen–Poiseuille flow: A spatial stability analysis," *Phys. Fluids* **14**, 3087 (2002).

³³F. Marques and J. M. Lopez, "Precessing vortex breakdown mode in an enclosed cylinder flow," *Phys. Fluids* **13**, 1679 (2001).

³⁴F. Marques, J. M. Lopez, and J. Shen, "Mode interactions in an enclosed swirling flow: A double Hopf bifurcation between azimuthal wavenumbers 0 and 2," *J. Fluid Mech.* **455**, 263 (2002).

³⁵J. M. Lopez, J. E. Hart, F. Marques, S. Kittelman, and J. Shen, "Instability and mode interactions in a differentially driven rotating cylinder," *J. Fluid Mech.* **462**, 383 (2002).

³⁶F. Marques, A. Yu. Gelfgat, and J. M. Lopez, "Tangent double Hopf bifurcation in a differentially rotating cylinder flow," *Phys. Rev. E* **68**, 016310 (2003).

³⁷J. M. Lopez, Y. D. Cui, and T. T. Lim, "Experimental and numerical investigation of the competition between axisymmetric time-periodic modes in an enclosed swirling flow," *Phys. Fluids* **18**, 104106 (2006).